



Investigation of impacts between unmanned aerial vehicle motors and various targets

Florian Franke^{1,2}, Uli Burger¹, Christian Hühne^{2,3}

¹ Technische Hochschule Ingolstadt, Esplanade 10, 85049 Ingolstadt, Germany

² Technische Universität Braunschweig, Universitätsplatz 2, 38106 Braunschweig, Germany

³ Deutsches Zentrum für Luft- und Raumfahrttechnik, Lilienthalplatz 7, 38108 Braunschweig, Germany

Abstract

Small unmanned aerial vehicles (sUAV) are an increasing threat for manned aircraft. Previous studies show that heavy and dense components of such sUAVs can severely damage aircraft structures. Therefore, this paper analyses the impact behavior of motors from a DJI Phantom 4 quadcopter with various targets. A FE model of this motor is also being developed. This analysis includes a stepwise test program, starting with quasi-static compression tests and end with high velocity impact tests on aluminium Al2024-T3 targets. In between there are high velocity impact tests on a rigid target. The FE model, developed for the explicit solver Radioss, is validated against the test data. We see that a single motor penetrates an aluminium sample at an impact velocity of 139.3 m/s, but does not perforate it. The impact of a single motor therefore may produce large structural damage to aircraft. Whether this damage has an effect on airworthiness must be investigated in further studies.

Keywords: Impact test, unmanned aerial vehicle, finite element model, drone impact, UAV

1. Introduction

The total amount of unmanned aerial vehicles (UAV) within the airspace grows. UAVs are taking on more and more tasks. These reach from parcel delivery to traffic monitoring, photography and further leisure activities. This results in an enhanced probability for airborne collisions, thereby UAVs are a safety concern for manned aviation [1, 2]. Within this paper, we use the term “drone strike”, first defined in Ref. [3], which describes an airborne collision between a manned and an unmanned aircraft. We focus on small unmanned aerial vehicles (sUAV) within the following investigations. An unmanned aerial vehicle with a maximum take-off weight (MTOW) of less than 25 kg is categorized as an sUAV [4].

Various researchers are working on investigations of drone strikes. The research group ASSURE “Alliance for System Safety of UAS through Research Excellence” performed an “UAS Airborne Collision Severity Evaluation” [5] and published corresponding technical volumes [4, 6, 7]. They developed validated finite element (FE) models for a DJI (Da-Jiang Innovations Science and Technology Co., Ltd) Phantom 3 quadcopter and a fixed-wing drone and investigated the airborne collision severity with fixed wing aircraft [1, 8]. ASSURE performed high-velocity impact tests with various UAV components on aluminium Al2024-T3 specimen to validate their FE models. Their main conclusion is that a drone strike, compared to a bird strike, will produce more damage to the aircraft structure. The Civil Aviation Safety Authority (CASA) determined the penetration speeds of various materials subjected to drone strikes [9]. Helicopters have a higher risk of mid-air collisions with sUAVs than fixed wing aircraft, according to the Civil Aviation Authority (CAA) [10]. Song and Schroeder published investigations of the ingestion of an sUAV into high-bypass engines [11–13]. According to their results, drones are a larger threat to high-bypass engines than these are certified for. Meng et

al. [14] conducted full scale impact tests and simulations with a DJI Inspire 1 drone on a horizontal stabilizer of a commercial airliner. They conclude that a commercial plane cannot safely continue its flight after a drone strike. Lu et al. [15] investigated drone strikes on windshields. They performed eight impact tests with five different sUAVs. They validated their FE simulations with these test data. Their conclusion is that mass, impact velocity, material and drone configuration have an influence on the damage size. Damage that would repeal the airworthiness occurs from 210 kJ. Jonkheijm [16] investigated drone strikes on helicopter windshields with LS-Dyna. He concluded that drones with a maximum take-off weight of 1.5 kg will crush current helicopter windshields [16], but he used questionable material data for the windshields. The modulus of elasticity for stretched acrylic material is too high. QinetiQ and EASA published a summary report about the “Vulnerability of manned aircraft to drone strikes” and analysed the current state of the art about drone strikes[17].

As it can be seen from this literature review, only ASSURE has conducted impact tests with individual UAV components [4]. In particular, components made of hard and dense materials can severely damage the target structures. ASSURE performed four high-velocity impact tests with DJI Phantom 3 motors against aluminium 2024-T3 panels. In this paper we investigate the impact behavior of the newer DJI Phantom 4 motors. This paper presents the test methods as well as data from quasi-static and impact investigations of these motors. We investigate impacts on rigid targets and aluminium Al2024-T3 flat panels. A finite element model of the projectile is validated with quasi-static and high-velocity impact test data. Finally, the results are discussed.

2. Methods

2.1 Experimental investigations

We investigate motors of the DJI Phantom 4 Series. DJI is the drone market leader and the Phantom 4 is one of the most sold sUAV within the open category [18]. It has a total mass of $m_{\text{drone}}=1387.0$ g and a maximum speed of $v_{\text{max}}=20.0$ m/s [19]. One motor (Figure 1) of this drone has an average mass of $m_{\text{M}}=53.0$ g. Its diameter is $d=28.2$ mm and its length is $l=36.0$ mm. We use both new and used motors for our investigations. The direction of rotation of the motor is neglected as it has no influence on the impact behavior.



Figure 1 – Investigated sUAV motors

We follow a stepwise structure and start at the quasi-static level with compression tests of the motors. Then we study high velocity impacts (HVI) on rigid target structures. Finally, HVI tests on deformable targets are investigated. We investigate high velocity impacts with a gas cannon. The quasi-static tests are performed on a ZwickRoell compression testing machine. We varied the orientation of the reinforcements (RF) of the motor, as shown in Figure 2. The “reinforcement upwards” configuration is expected to be stiffer since the strut is in the direction of the compressive force. We assume that there is no difference in the upwards and a downwards direction of the reinforcement. The same is assumed for the sideways orientation. We performed five tests with the radial reinforcements upwards, three tests with the radial reinforcement sideways and three tests in longitudinal direction.

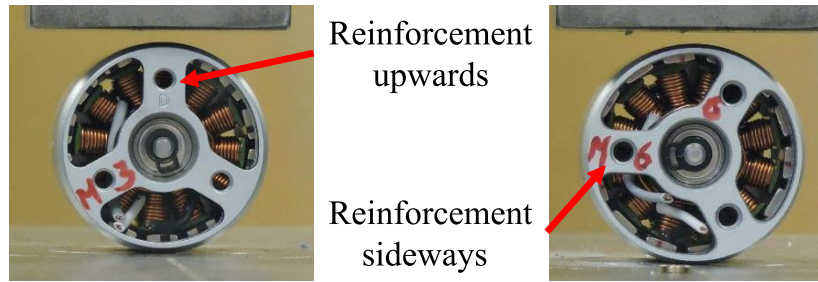


Figure 2 - Positions of reinforcements

Figure 3 shows a model of the gas cannon device. The projectile lies within a sabot. The sabot is accelerated along the tube with pressurized air when the valve opens. The impact velocity can be adjusted via pressure in the tank. The interceptor separates the projectile from the sabot. A light barrier measures the impact velocity. Four 100 kN piezo force measurement cells are used to measure the impact force. The high-speed camera “Photron Nova S12” records the impact with 30000 frames per second. The deflections of the projectile are evaluated with the open source software Tracker 5.1.4. We track the deflection of the rear edge of the motor bottom side. 18 impact tests are performed on the rigid target with a mean mass of the motor $m_M=53.0$ g and velocities between $v_0=22.0$ m/s and 103.0 m/s. Table 1 lists all impact tests on the rigid target with the measured velocity of the projectile.

Table 1 - Impact tests on rigid wall

Test	Series	m_M [g]	v_0 [m/s]	E_{kin} [J]
RW-1	1	52.9	23.6	14.7
RW-2	1	53.2	25.3	17.0
RW-3	1	52.9	26.8	18.9
RW-4	2	53.5	29.7	23.6
RW-5	2	53.1	29.3	22.8
RW-6	2	52.9	32.2	27.4
RW-7	3	52.9	42.4	47.5
RW-8	3	52.8	41.6	45.6
RW-9	3	53.0	41.7	46.1
RW-10	4	52.9	51.6	70.5
RW-11	4	53.1	50.7	68.3
RW-12	4	52.8	55.8	82.3
RW-13	5	53.0	82.7	181.3
RW-14	5	53.0	88.4	207.0
RW-15	5	53.2	81.3	175.9
RW-16	6	53.1	93.3	231.0
RW-17	6	53.0	100.2	266.2
RW-18	6	52.9	99.0	259.1

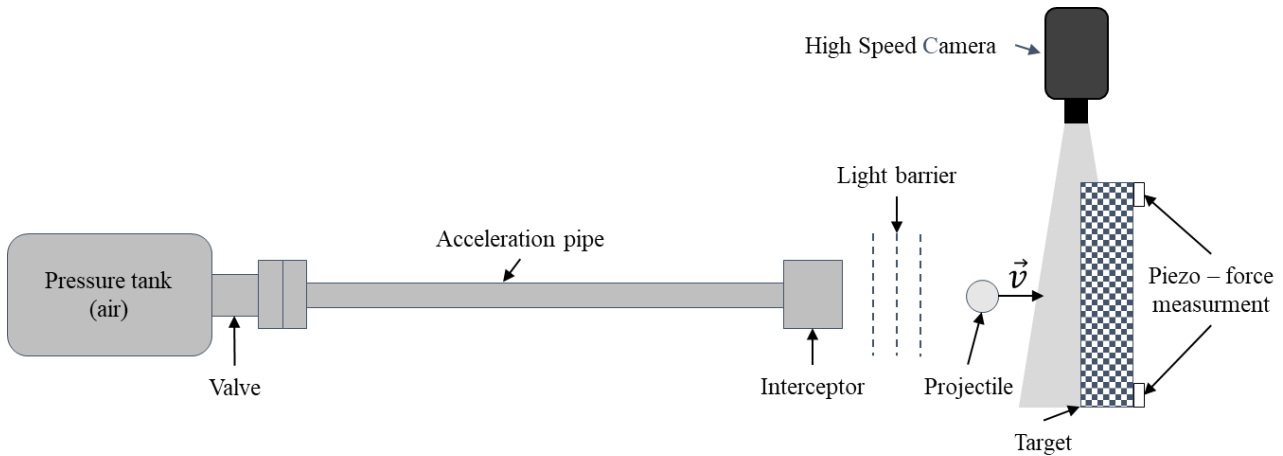


Figure 3 - Model of gas cannon test device

Finally, four impact tests on a deformable target are conducted (Table 2). The impact speeds are between $v_0=79.9$ m/s and 139.3 m/s. We use the same gas cannon as for the rigid wall tests. Only the target is different. The targets are aluminium Al2024-T3 flat panels (385.0 mm x 290.0 mm x 2.54 mm). Al2024-T3 is being studied as it is a standard aerospace material. The samples are fixed all around with 14 M8 countersunk screws in a so-called picture frame. The unsupported area is therefore 275.0 mm x 175.0 mm. Figure 4 shows the deformable target within the picture frame.

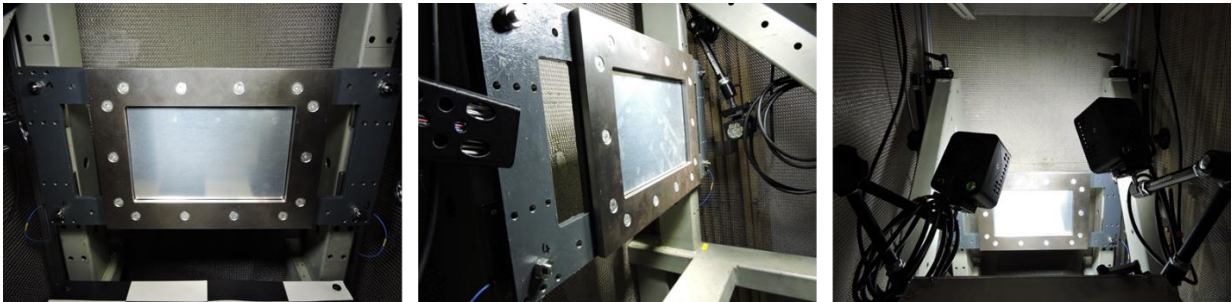


Figure 4 - Flexible target within the target picture frame

Table 2 - Impact tests on deformable targets

Test	m_M [g]	v_0 [m/s]	E_{kin} [J]
FT1-1	52.7	97.5	250.5
FT1-2	53.0	113.6	342.0
FT1-3	52.7	139.3	415.7
FT1-4	52.8	79.9	168.5

2.2 Numerical Models

The FE model of the drone motor consists of five subcomponents: Case top- and bottom side, shaft, stator and magnets. All components are meshed with solid elements (/PROP/TYPE14). A standard 8-node solid element with full integration (H8C) is used. It is assumed that the outer shell of the motor is made of an aluminum-magnesium cast alloy (AlMg3), comparable to the ASSURE model of the DJI Phantom 3 motor. The stator of the electric motor is a M530-50A steel. The stator is wound with a coil of copper, which is neglected in the simulation model. ASSURE assumes that the motor shaft consists of aluminum cast alloy. Reverse engineering of the motor reveals that the shaft is made of steel. We assume a simple AISI 1006 steel, since the shaft has only a minor influence on the global deformation. The general contact /INTER/TYPE7 is used for contact modelling between the components. The

model consists of a total of 37999 nodes and 25056 elements. Figure 5 shows the FE model of the motor.

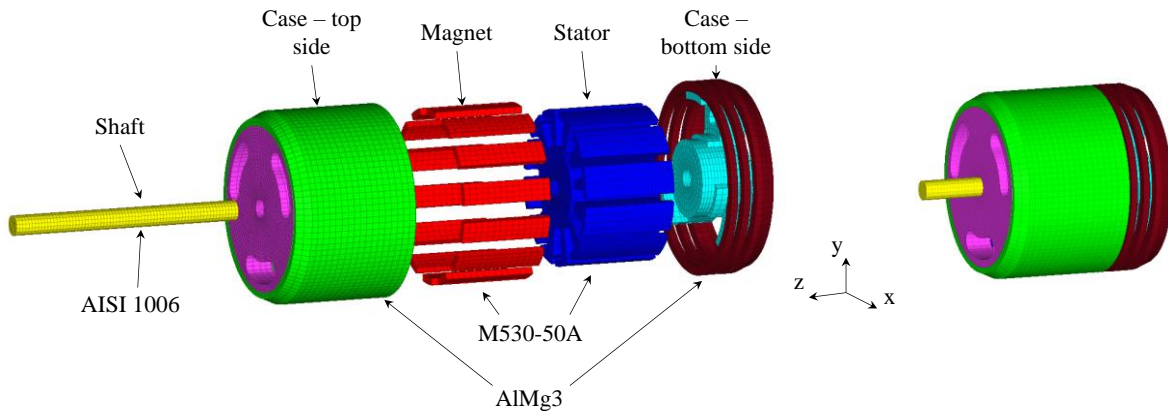


Figure 5 - FE model of an sUAV motor with corresponding materials

Both target structures from the impact tests are transferred to FE models. Figure 6 shows the model of the rigid wall. It consists of nine subcomponents and three materials. The adapter plates are made of S235 steel with elastic behavior. The plate consists of four arms as well as a back and a front side. Between the adapter plates and the rigid plate are the load cells, which are modelled as beam elements. The material used is S235. All arms as well as the back side are modelled with AISI422+S purely elastic. The front side is modeled with the Johnson-Cook model. The model consists of 34836 H8C fully integrated solid elements, 3571 fully integrated QEPH shell elements as well as 40 beam elements and a total of 47373 nodes.

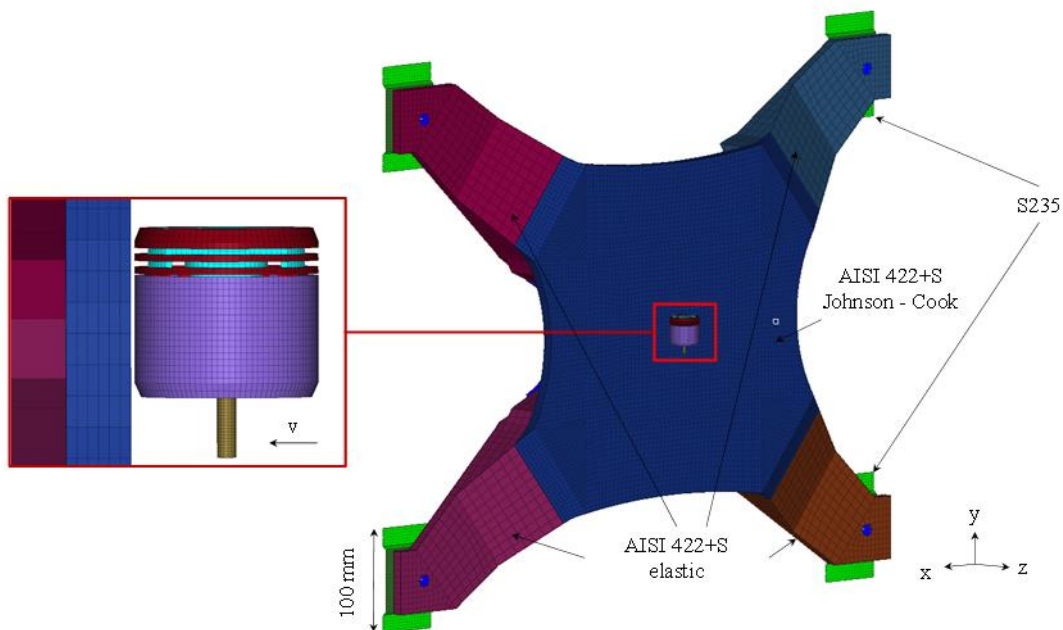


Figure 6 - FE model rigid wall

Figure 7 shows the FE model for deformable targets. Base frame and picture frame are made of AISI 4140 steel with the Johnson-Cook material model. The sample material is aluminum AI2024-T3, also with Johnson-Cook model. The model consists of 29238 H8C solid elements, 22040 QEPH shell elements and 14 beam elements.

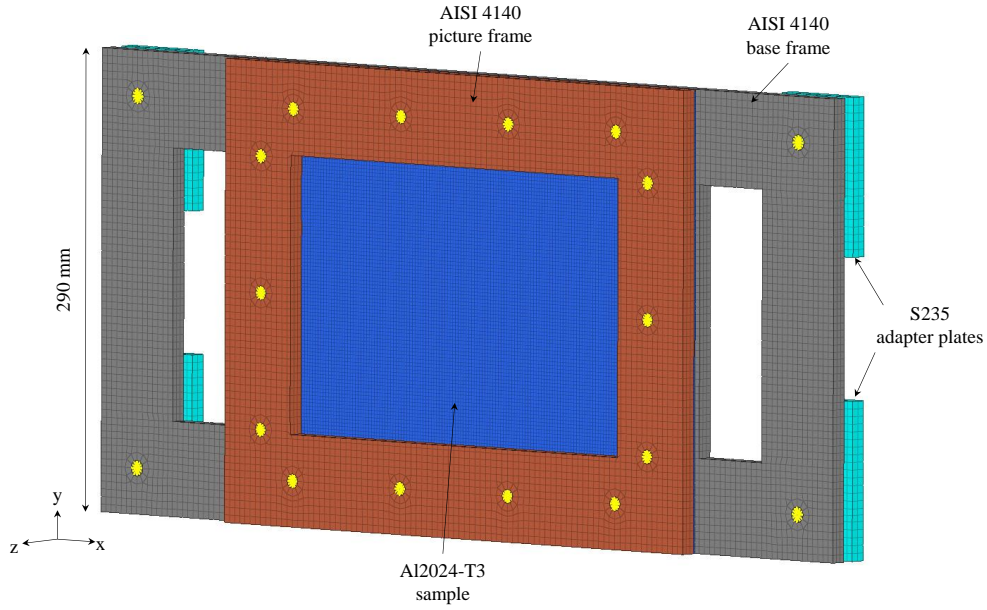


Figure 7 - FE model picture frame for aluminum AL2024-T3 targets

The Johnson-Cook constitutive model in equation (1) is used for the materials listed in Table 3.

$$\sigma_y(\varepsilon_p, \dot{\varepsilon}_p, T) = \left[a + b(\varepsilon_p)^n \right] \left[1 + c \ln \left[\frac{\dot{\varepsilon}_p}{\dot{\varepsilon}_{p0}} \right] \right] \left[1 - \left(\frac{T - T_0}{T_m - T_0} \right)^m \right] \quad (1)$$

The function for determining the yield stress σ_y consists of three terms. The first term is used to model the hardening. The parameter a is the initial yield stress, b represents a strain hardening constant and n the strain hardening coefficient. The parameter c is the strengthening coefficient of strain rate, $\dot{\varepsilon}_{p0}$ is a reference strain rate. The last term includes the thermal softening with m as the softening coefficient. T_0 represents a reference temperature, such as room temperature, T_m is the melting temperature of the material [20–22].

Table 3 - Material properties and Johnson-Cook parameters for different materials

	ρ [kg/m ³]	E [MPa]	ν	a [MPa]	b [MPa]	n	c	m	$\dot{\varepsilon}_{p0}$	Source
AlMg3	2700	68000	0.3	28.13	278.67	0.183	0.00439	2.527	0.1	[23]
Al2024-T3	2770	73000	0.33	369	684	0.73	0.0083	1.7	1	[24]
AISI 1006	7872	190000	0.3	350	275	0.36	0.022	1.0	1	[20]
AISI 4140	7850	219000	0.29	595	580	0.133	0.023	1.03	1	[25]

The Johnson-Cook damage model in equation (2) is used to model the damage.

$$\varepsilon_{fail} = \left[D_1 + D_2^{(D_3 \sigma^*)} \right] \left[1 + D_4 \ln \left[\frac{\dot{\varepsilon}_p}{\dot{\varepsilon}_{p0}} \right] \right] \left[1 + D_5 \left(\frac{T - T_0}{T_m - T_0} \right) \right] \quad (2)$$

The values for D_1 to D_5 have to be determined empirically. We use the following parameters, listed in Table 4.

Table 4 - Parameters for Johnson-Cook damage model for Radioss

	D1	D2	D3	D4	D5	Source
AlMg3	-0.2	1.133	-0.229	0.0897	7.978	[23]
Al2024-T3	0.112	0.123	-1.5	0.007	0	[24]
AISI 1006	-0.8	2.1	-0.5	0.002	0.61	[20]

Radioss offers the possibility that Johnson-Cook parameters are determined internally via the solver from yield strength, tensile strength and elongation at break. This option is used for M530-50A and AISI 422+s with the following parameters in Table 5. In addition, the data for purely elastic behavior are listed in Table 6:

Table 5 - Elasto-plastic material parameters

	$\rho \left[\frac{kg}{m^3} \right]$	$E [MPa]$	ν	$R_{p02} [MPa]$	$R_m [MPa]$	$\varepsilon_{max} [-]$	Source
M530-50A	7700	210000	0.3	295	430	0.89	[26]
AISI 422+s	7750	207000	0.3	735	880	0.25	[27]
PC	1180	2350	0.3	62	62	0.2	[14]

Table 6 - Purely elastic behavior

	$\rho \left[\frac{kg}{m^3} \right]$	$E [MPa]$	ν
S235	7850	210000	0.3
AISI422+s	7750	207000	0.3

3. Results & Discussion

3.1 Quasi-static compression tests

Figure 8 shows the force–deflections curves for three test series in a) to c). The mean values with corresponding standard deviations for different motor orientations under quasi-static compression loads are presented in Figure 8 d). Three points should be highlighted for the tests in the radial direction:

- load redistribution at $u = 0.65$ mm due to contact of the stator with the outer aluminum shell
- crack initiation at $u = 2.1$ mm, which leads to a change in the slope of the force-displacement curve
- load redistribution at $u = 7.5$ mm by closing the cooling air holes on the upper motor side

The load redistribution due to the closing of the cooling air holes is more pronounced for the orientation "RF upwards" as there is no hole in the direction of the acting compressive force for the orientation "RF sideways". Comparing the results for the upwards and sideways oriented reinforcement, it can be seen that the curves overlap within the range of the standard deviations. Consequently, the position of the reinforcement will be neglected for further investigations.

In the longitudinal direction, two load redistributions appear. The first occurs at $u = 0.4$ mm due to the failure of the shaft bearing. At a displacement of $u = 2.7$ mm, on the one hand the mounting of the rotor buckles, and on the other hand the slat of the bottom closes. In order for motors to impact the target in the longitudinal direction, the drone must rotate 90° around the transverse axis. This case is considered unlikely, which is why only test data in the radial direction is used in the following.

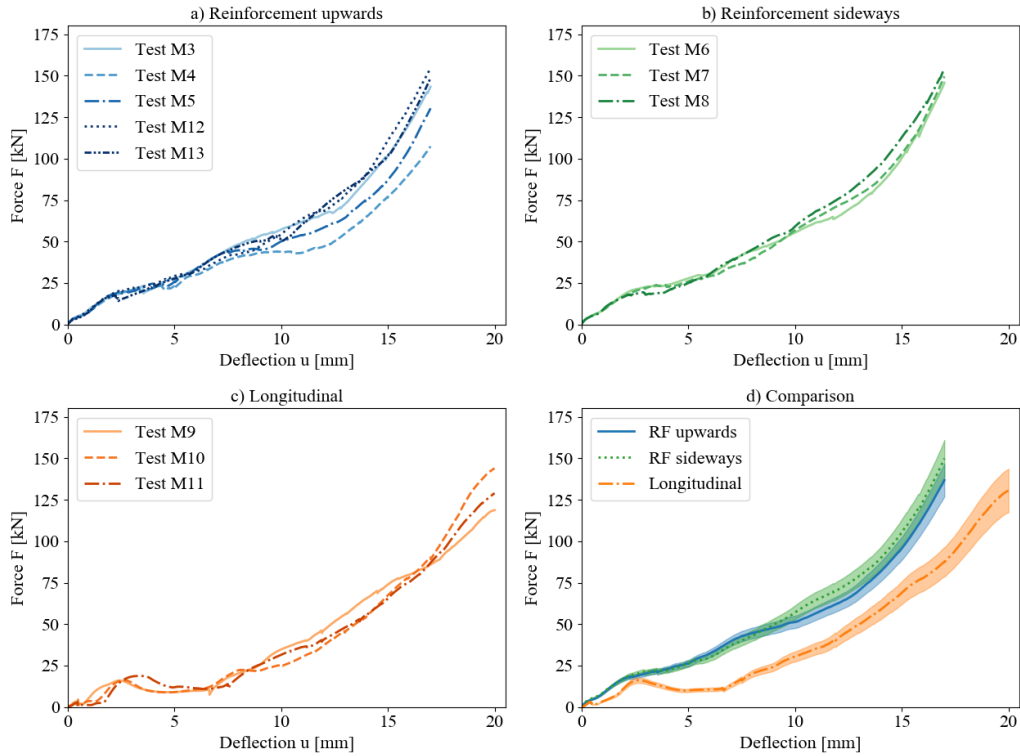


Figure 8 - Force-deflection curves under quasi-static compression load for various motor configurations

For validation of the FE model, we vary the material model of aluminium (Figure 9 a), the loading speed (Figure 9 b) and the stator material (Figure 9 c). With the Johnson-Cook model, a loading speed of 3 m/s and the stator material M530-50A, the FE models show the smallest deviations from the real tests (Figure 9 d) and a good numerical efficiency. Only the range between 2.1 mm and 7.5 mm is above the test data. This is due to the material of the stator, as diagram c) shows.

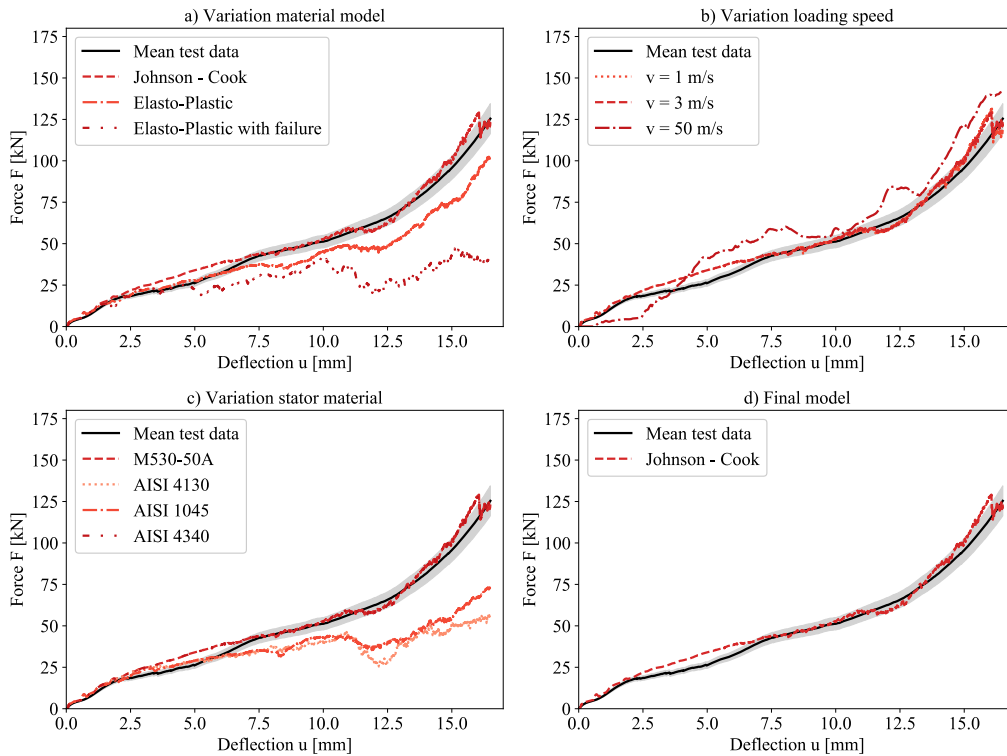


Figure 9 - FE data of quasi-static compression tests

3.2 High velocity impact on rigid wall

We compare the quasi-static test results with force–deflection data from high velocity impact (HVI) tests in Figure 10 as well as FE data from HVI simulations. The deflections of the projectiles are determined by analysis of the high-speed videos. The rear edge of the motor is tracked and used as the deflection u . The impact is recorded with 30000 frames per second (fps). We interpolate between the data points to determine a deflection signal. On the one hand, this explains the scattering along the x axis. On the other hand, the motor does not always hit perfectly vertically, which leads to further scattering. We see that the HVI tests show good agreement with the quasi-static data up to series 4. Tests RW-4, RW-9 and RW-10 represent outliers in this context, as they did not hit the target vertically.

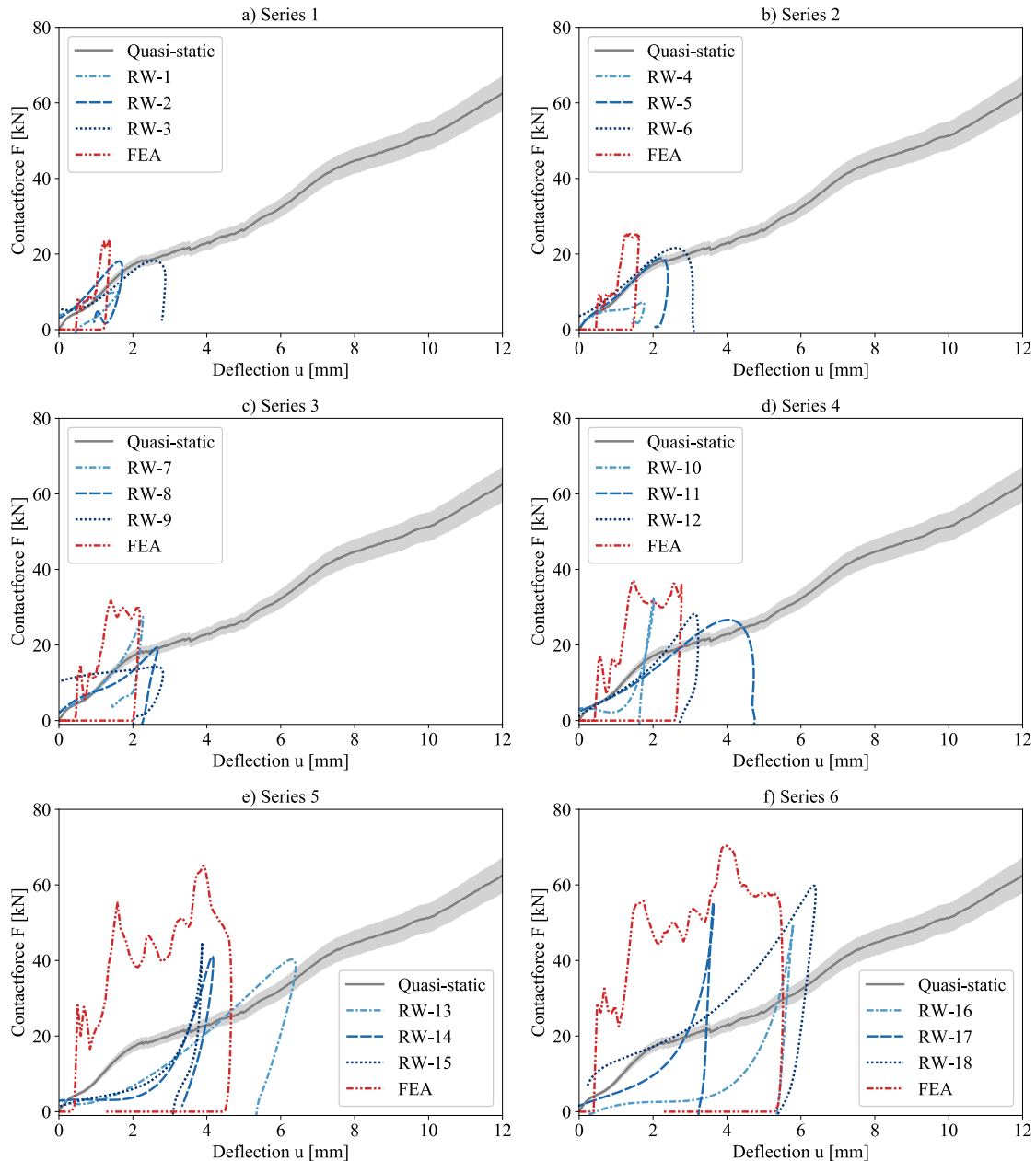


Figure 10 - Force-Deflection curves for high velocity impact tests compared to quasi-static and FEA results

Test series with higher impact energies (series 5 and 6) show greater deviations from the quasi-static data. In contrast, the FE data show curves that deviate from the quasi-static and HVI test data. The measurement method leads to these strong deviations. We measure the deflection in the tests with point tracking within the high-speed videos. The videos are recorded with 30000 fps but only 6 to 12 pictures show the real impact process. These points are used as base points and interpolation is

performed between them. The trailing edge of the motor is tracked. In the simulations, a longitudinal line is formed along which the mean value of the deflection is determined. In all simulations we observe a steep increase in force as soon as the motor strikes. The force reaches a first load peak that is between 37 and 46.2 % of the maximum force before it drops again or forms a plateau. This is followed by a second steep load increase. The length of the first plateau is the same for all simulations. The second rise as well as the maximum force must therefore be generated by the impact of the stator. Drops in the force curve indicate damage to the motor projectile.

3.3 High velocity impact on aluminium Al2024-T3 targets

The final test series are impact tests on aluminium Al2024-T3 flat panels. We perform four impact tests with $v_i=79.9, 97.5, 113.6$ and 139.3 m/s. Figure 11 shows the force–deflection curves for these tests and FEA results. Impacts with the highest velocities (Figure 11 c and d) show a higher peak force than impacts with a lower velocity. Regardless the velocity difference of $\Delta v_0=25.7$ m/s between FT1-3 and FT1-2 the force maxima of both tests are equal. There are two differences between these two tests. On the one hand, the deflection of FT1-3 is with $u=43.3$ mm greater than the deflection of FT1-2 with $u=19.9$ mm. On the other hand, FT1-3 is the only test that shows a penetration damage after impact. We see in Figure 12 that the impact area opens up for this test and forms a petaling damage. The FEA data deviates from the test data. These curves show a high peak immediately after the first contact. This peak decays within a deflection of 0.1 mm. This is a numerical effect due to the contact definition. This initial peak is followed by a first local force maximum. After this maximum, the force curve shows a decrease before it rises to a second local maximum. After that, the force drops to 0 N. Smaller rises in the curve occur due to rebounds. The difference between the flexible and rigid target is that the second peak is not as pronounced as for impacts on the rigid wall. Compared to the test data, the deflections are smaller. The force maxima of the tests are below the local maxima of the test data, whereby the deviations increase with the impact speed. The test data were determined purely optically, which is why we have more accurate results from the FE models.

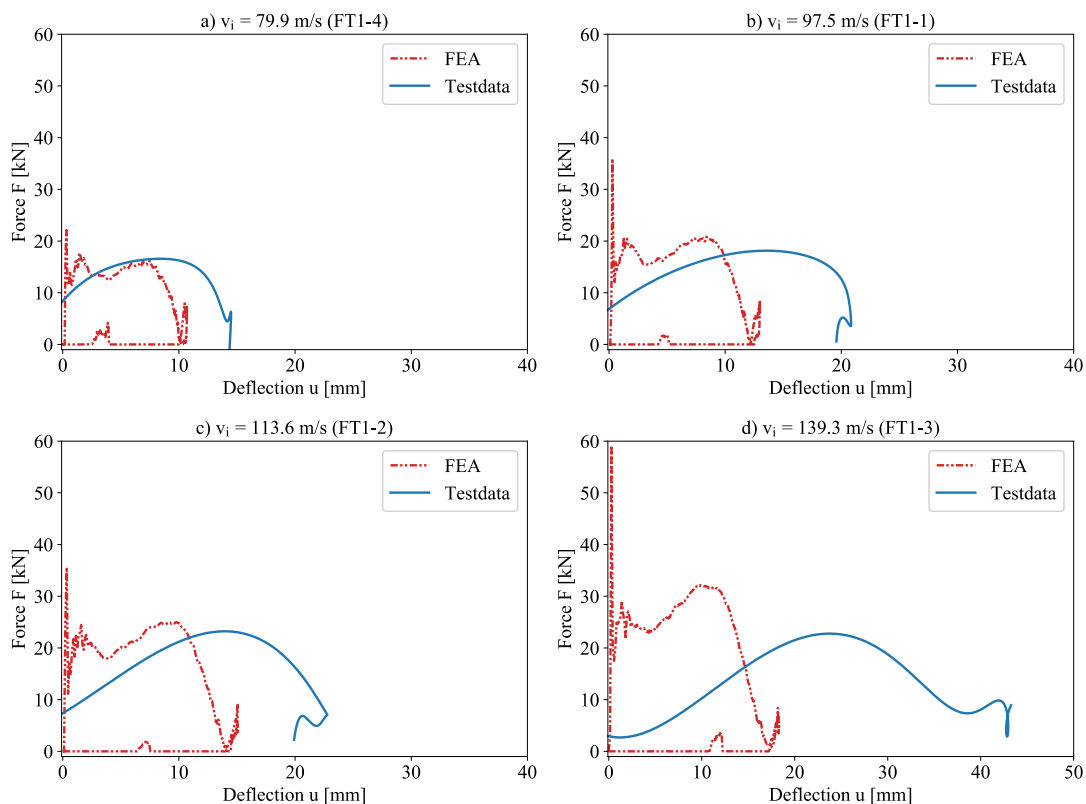


Figure 11 - Force-Deflection curves from tests and FEA for impacts on Al2024-T3 panels

Figure 12 shows the Al2024-T3 targets and motor projectiles after impact. The FE models are also shown in comparison. The motors do not perforate the targets regardless of the speed. Damage to

the target structure occurs both in the tests and in the simulations for the largest impact velocity. The width of the damage of the FE model is 40.5 mm, which is smaller than the damage size in the tests, which is 75.0 mm (Figure 13). The projectile is tilted about the transverse axis in the tests and hits the target offset from the specimen center, which can explain the deviations.




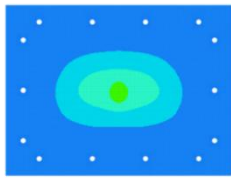
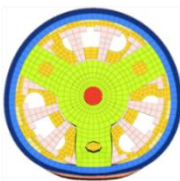
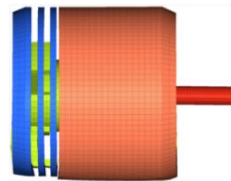



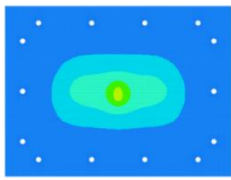

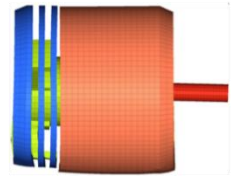


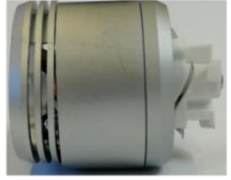
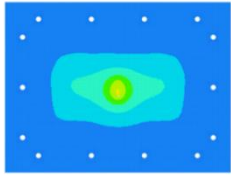

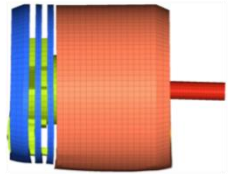



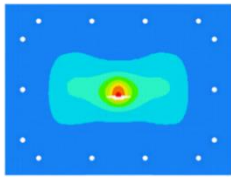

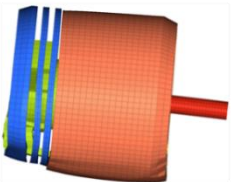
$v_i \left[\frac{m}{s} \right]$		Al2024-T3 Front	Motor	
79.9	Test			
	FEA			
97.5	Test			
	FEA			
113.6	Test			
	FEA			
139.3	Test			
	FEA			

Figure 12 - Test specimen and FE models after impact

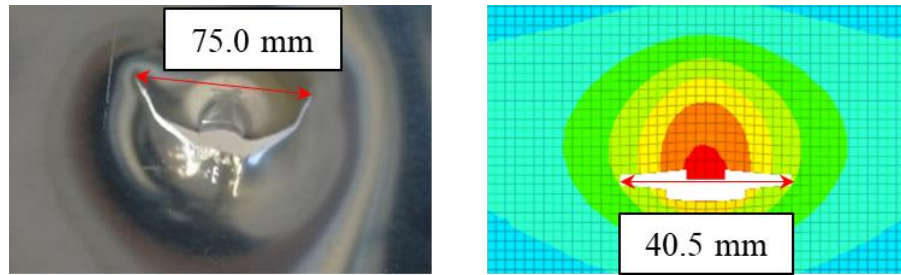


Figure 13 - Damage sizes of test and simulation for an impact velocity of $v_i=139.3$ m/s

We see, that a single motor is able to produce significant damage to aluminium panels. The considered speed range is realistic and can be reached in the vicinity of e.g. airports. The damage of the structure also depends on the material. Structures made of composite materials, for example, tend to delaminate. Other materials will show greater damage as aluminium usually has good impact properties and shows smaller damage than composites. It must be emphasized that only the impact of a single motor is considered here. The full drone strike will produce even greater damage to the target structure, as the mass of the projectile is significantly greater. Besides the motors, a drone consists of other components such as the battery, payload, etc. All these components have an effect on the impact process. The drone strike thus represents a multi-body impact. The impact of additional components and the interaction between components need to be investigated in further studies.

4. Conclusion

This paper presents test as well as FE simulation data from quasi-static and impact tests of sUAV motors on rigid targets and aluminum Al2024-T3 specimen. The motor FE model is validated using the quasi-static data. We found that impacts with a low energy (up to 42 J) are comparable to quasi-static results. Higher impact energies lead to larger deviations in the force-deflection curves between quasi-static and impact tests. A single motor of a drone is able to penetrate an Al2024-T3 structure at a speed of 139.3 m/s. Only the impact of a single motor is studied within this paper. A full drone may produce even greater damage to the targets, with serious consequences to the aircraft.

Results from this paper enable first estimations of possible damage and threat scenarios by investigation of deformable targets for HVI. Furthermore, we gain an in-depth knowledge of damage behavior of sUAV motors under different velocity regimes. In comparison to the existing literature, we have created a data basis for impact tests of sUAV motors. The data from those test series may be used for further investigations as well as validations of impact simulations of sUAV motors. Further test series on other material samples are needed as well as investigations of different sUAV motor sizes in order to obtain a comprehensive database.

5. Acknowledgments & Funding

We would like to thank Michael Schwab, Prof. Ludwig König, Volker Oberländer and Yvonne Hadinger for their support during the experiments.

This research work is financed by the German Federal Ministry of Education and Research within the funding program "Forschung an Fachhochschulen" under the contract sign DESIRE – 13FH581IX6.

6. Contact Author Email Address

Contact: Florian.Franke@thi.de; Uli.Burger@thi.de

7. Copyright Statement

The authors confirm that they, and/or their company or organization, hold copyright on all of the original material included in this paper. The authors also confirm that they have obtained permission, from the copyright holder of any third party material included in this paper, to publish it as part of their paper. The authors confirm that they give permission, or have obtained permission from the copyright holder of this paper, for the publication and distribution of this paper as part of the AEC proceedings or as individual off-prints from the proceedings.

9. References

- [1] K. R. Kota, T. Ricks, L. Gomez, J. E. d. I. Monteros, G. Olivares, and T. E. Lacy, "Development and validation of finite element impact models of high-density UAS components for use in air-to-air collision simulations," *Mechanics of Advanced Materials and Structures*, pp. 1–22, 2020, doi: 10.1080/15376494.2020.1740956.
- [2] R. Weibel and R. J. Hansman, "Safety Considerations for Operation of Different Classes of UAVs in the NAS," in *AIAA 4th Aviation Technology, Integration and Operations (ATIO) Forum*, Chicago, Illinois. Accessed: Feb. 15 2017.
- [3] F. Franke, M. Schwab, and Burger, Uli, Hühne, Christian, "An Analytical Approach to Determine the Impact Force of Small Unmanned Aerial Vehicle Collisions with Rigid and Elastic Targets," in *Proceedings of the 1. Aerospace Europe Conference 2020*, Bordeaux, 2020.
- [4] O. Gerardo, L. Gomez, J. Espinosa, R. Baldrige, C. Zinzuwadia, and T. Aldag, "Volume II - UAS Airborne Collision Severity Evaluation: Quadcopter," FAA, Springfield, UAS Airborne Collision Severity Evaluation 2, Jul. 2017. Accessed: Nov. 29 2017. [Online]. Available: <http://www.assureuas.org/projects/deliverables/a3/Volume%20II%20-%20UAS%20Airborne%20Collision%20Severity%20Evaluation%20-%20Quadcopter.pdf>
- [5] O. Gerardo *et al.*, "UAS Airborne Collision Severity Evaluation: Executive Summary - Structural Evaluation," FAA, Springfield, UAS Airborne Collision Severity Evaluation, Jul. 2017. Accessed: Nov. 29 2017. [Online]. Available: <http://www.assureuas.org/projects/deliverables/a3/Volume%20I%20-%20UAS%20Airborne%20Collision%20Severity%20Evaluation%20-%20Structural%20Evaluation.pdf>
- [6] O. Gerardo *et al.*, *Volume III - UAS Airborne Collision Severity Evaluation: Fixed-Wing*. [Online]. Available: <http://www.assureuas.org/projects/deliverables/a3/Volume%20III%20-%20UAS%20Airborne%20Collision%20Severity%20Evaluation%20-%20Fixed-wing.pdf> (accessed: Nov. 29 2017).
- [7] K. D'Souza, T. Lyons, T. Lacy, and K. R. Kota, "Volume IV - UAS Airborne Collision Severity Evaluation: Engine Ingestion," FAA, Springfield, UAS Airborne Collision Severity Evaluation, Jul. 2017. Accessed: Nov. 29 2017. [Online]. Available: <http://www.assureuas.org/projects/deliverables/a3/Volume%20IV%20-%20UAS%20Airborne%20Collision%20Severity%20Evaluation%20-%20Engine%20Ingestion.pdf>
- [8] K. R. Kota, "Development and Verification of a Finite Element Model of a Fixed-Wing Unmanned Aerial System for Airborne Collision Severity Evaluation," Ph.D, Mississippi State University, Ann Arbor, 2018. [Online]. Available: <https://www.proquest.com/docview/2100708118?accountid=135362>
- [9] A. Radi, "Potential damage assessment of a mid-air collision with a small UAV," Civil Aviation Safety Authority, Jun. 2013. Accessed: Oct. 4 2016. [Online]. Available: <https://www.casa.gov.au/files/potential-damage-assessment-mid-air-collision-small-rpapdf>
- [10] P. David, "Drone Safety Risk: An assessment: CAP 1627," Civil Aviation Authority, Gatwick, 2018. Accessed: May 11 2018.
- [11] Y. Song, K. Schroeder, B. Horton, and J. Bayandor, "Advanced Propulsion Collision Damage due to Unmanned Aerial System Ingestion," in *30th Congress of the International Council of the Aeronautical Sciences*, Seoul, 2016.
- [12] Y. Song, B. Horton, and J. Bayandor, "Investigation of UAS Ingestion into High-Bypass Engines, Part 1: Bird vs. Drone," in *AIAA SciTech Forum, 58th AIAA/ASCE/AHS/ASC Structures, Structural Dynamics, and Materials Conference: American Institute of Aeronautics and Astronautics*, 2017.
- [13] K. Schroeder, Y. Song, B. Horton, and J. Bayandor, "Investigation of UAS Ingestion into High-Bypass Engines, Part 2: Parametric Drone Study," in *AIAA SciTech Forum, 58th AIAA/ASCE/AHS/ASC Structures, Structural Dynamics, and Materials Conference: American Institute of Aeronautics and Astronautics*, 2017.
- [14] X. Meng *et al.*, "Dynamic response of the horizontal stabilizer during UAS airborne collision," *International Journal of Impact Engineering*, vol. 126, pp. 50–61, 2019, doi: 10.1016/j.ijimpeng.2018.11.015.
- [15] X. Lu, X. Liu, Y. Li, Y. Zhang, and H. Zuo, "Simulations of airborne collisions between drones and an aircraft windshield," *Aerospace Science and Technology*, p. 105713, 2020, doi:

- 10.1016/j.ast.2020.105713.
- [16] L. Jonkheijm, "Predicting helicopter damage caused by a collision with an Unmanned Aerial System using explicit Finite Element Analysis," Masterthesis, Technical University Delft, Delft, 2020. [Online]. Available: <http://resolver.tudelft.nl/uuid:90105518-e3f8-4355-b9d3-bf541215e83c>
- [17] W. J. Austen, S. J. Lord, and S. A. Bridges, *Vulnerability of manned aircraft to drone strikes: Research Project EASA.2020.C04*. [Online]. Available: https://www.easa.europa.eu/sites/default/files/dfu/deliverable-analysis_of_the_state-of-the-art_d1.3_and_research_cooperation_d1.4.pdf (accessed: Nov. 5 2020).
- [18] Skylogic Research, *2018 Drone Market Sector Report: Opportunities and challenges in key market segments*. [Online]. Available: <http://droneanalyst.com/research/research-studies/2018-drone-market-sector-report-purchase> (accessed: Jan. 9 2019).
- [19] DJI, *Phantom 4: Bedienungsanleitung*. [Online]. Available: https://dl.djicdn.com/downloads/phantom_4/de/DE_Phantom_4_User_Manual_v1.2_20160503.pdf
- [20] C. Lakshmana Rao, K. R. Y. Simha, and V. Narayanamurthy, *Applied impact mechanics*. Chichester, United Kingdom: Wiley, 2016. [Online]. Available: <http://onlinelibrary.wiley.com/book/10.1002/9781119241829>
- [21] G. R. Johnson and W. H. Cook, "A Constitutive Model and Data for Metals Subjected to Large Strains, High Strain Rates, and High Temperatures," in *Proceedings 7th International Symposium on Ballistics*, The Hague, 1983, pp. 541–547.
- [22] M. Murugesan and D. W. Jung, "Johnson Cook Material and Failure Model Parameters Estimation of AISI-1045 Medium Carbon Steel for Metal Forming Applications," *Materials (Basel, Switzerland)*, vol. 12, no. 4, 2019, doi: 10.3390/ma12040609.
- [23] M. Rodriguez-Millan, D. Garcia-Gonzalez, A. Rusinek, and A. Arias, "Influence of Stress State on the Mechanical Impact and Deformation Behaviors of Aluminum Alloys," *Metals*, vol. 8, no. 7, p. 520, 2018, doi: 10.3390/met8070520.
- [24] D. Ivančević, I. Smojver, and M. Leko, "Numerical Approach in the Evaluation of Aeronautical Structures Ballistic Protection," *Transportation Research Procedia*, vol. 35, pp. 190–199, 2018, doi: 10.1016/j.trpro.2018.12.029.
- [25] M. Agmell, A. Ahadi, and J.-E. Ståhl, "The Link Between Plasticity Parameters and Process Parameters in Orthogonal Cutting," *Procedia CIRP*, vol. 8, pp. 224–229, 2013, doi: 10.1016/j.procir.2013.06.093.
- [26] Cogent Power Ltd, *Electrical Steel Non Oriented Fully Processed*. [Online]. Available: <https://perso.uclouvain.be/ernest.matagne/ELEC2311/T2006/NOFP.pdf> (accessed: Mar. 11 2021).
- [27] Matweb, *AISI 422*. [Online]. Available: <http://www.matweb.com/search/DataSheet.aspx?MatGUID=81eb6302cf6a41eda0afa0a2afa8a203&ckck=1> (accessed: Mar. 11 2021).